

Research Article

Region-Based Segmentation and Wiener Pilot-Based Novel Amoeba Denoising Scheme for CT Imaging

Syed Muhammad Umar Talha ^{1,2}, Tariq Mairaj ¹, Waleed Bin Yousuf ¹
and Jawwad Ali Zahed ¹

¹Department of Electrical Engineering, Pakistan Navy Engineering College, National University of Sciences and Technology, H-12 Islamabad, Pakistan

²Department of Telecommunication Engineering, Sir Syed University of Engineering & Technology, Karachi, Pakistan

Correspondence should be addressed to Syed Muhammad Umar Talha; umar.talha@pnec.nust.edu.pk

Received 13 May 2020; Revised 28 September 2020; Accepted 21 November 2020; Published 14 December 2020

Academic Editor: Sacha Gómez

Copyright © 2020 Syed Muhammad Umar Talha et al. This is an open access article distributed under the Creative Commons Attribution License, which permits unrestricted use, distribution, and reproduction in any medium, provided the original work is properly cited.

Computed tomography (CT) is one of the most common and beneficial medical imaging schemes, but the associated high radiation dose injurious to the patient is always a concern. Therefore, postprocessing-based enhancement of a CT reconstructed image acquired using a reduced dose is an active research area. Amoeba- (or spatially variant kernel-) based filtering is a strong candidate scheme for postprocessing of the CT image, which adapts its shape according to the image contents. In the reported research work, the amoeba filtering is customized for postprocessing of CT images acquired at a reduced X-ray dose. The proposed scheme modifies both the pilot image formation and amoeba shaping mechanism of the conventional amoeba implementation. The proposed scheme uses a Wiener filter-based pilot image, while region-based segmentation is used for amoeba shaping instead of the conventional amoeba distance-based approach. The merits of the proposed scheme include being more suitable for CT images because of the similar region-based and symmetric nature of the human body anatomy, image smoothing without compromising on the edge details, and being adaptive in nature and more robust to noise. The performance of the proposed amoeba scheme is compared to the traditional amoeba kernel in the image denoising application for CT images using filtered back projection (FBP) on sparse-view projections. The scheme is supported by computer simulations using fan-beam projections of clinically reconstructed and simulated head CT phantoms. The scheme is tested using multiple image quality matrices, in the presence of additive projection noise. The scheme implementation significantly improves the image quality visually and statistically, providing better contrast and image smoothing without compromising on edge details. Promising results indicate the efficacy of the proposed scheme.

1. Introduction

Computed tomography (CT) has served as a fundamental tool for human internal anatomy visualization since its development and subsequent commercialization; with considerable benefits for mankind [1–6]. In radiology, CT uses projections from multiple cross-sectional views; consequently, patients are subjected to extensive radiation exposure. Although CT is a very informative medical diagnosis tool, the high radiation dose is a concern due to the associated hazards [2, 7, 8]. However, the reduction of radiation dose degrades the reconstructed image quality in most com-

monly used CT reconstruction algorithms. Developing techniques for CT reconstruction with reduced radiation dose is an active research area. Various strategies have been adopted to reduce the radiation dose, such as automatic exposure control, adjusting kV with respect to the patient or organ-specific dose, protocol optimization, postprocessing, advanced reconstruction techniques, limited data, and few-view techniques, etc. [2, 8–16]. Many advanced CT scanner designs have also been developed to support dose reduction, such as interior CT, low-dose CT, and sparse-view CT [17–19].

Sparse-view CT is a particular type of CT scans where the number of data acquisition views is reduced, while keeping

the X-ray tube current at the standard level. The sparse-view CT benefits in reducing radiation dose and scan time in cardiac CT [17]. Moreover, other sparse-view CT applications are micro-CT (for small animal imaging), flat panel detector, 3D angiography, and other industrial CT applications [17, 19–21]. However, conventional CT reconstruction algorithms, such as filtered back projection (FBP), are designed for densely sampled angular projections. Therefore, such algorithms do not produce diagnostic quality reconstructed images in sparse-view CT. The features in the reconstructed images can be enhanced through postprocessing; in which image processing techniques are widely used. Sophisticated image processing techniques offer a potential to extract more enhanced features from the reconstructed CT images.

Amoeba-based filtering [22] schemes have been a revolutionary contribution in image filtering applications. Amoeba is a spatially variant filter kernel which adapts its shape according to the image contents, intending to preserve edge details and contour boundaries while smoothing the degraded image segments. Amoeba-based filtering and its variants have been applied in many image processing applications such as adaptive neighborhood morphology (Debayle and Pinoli 2005), bilateral structuring functions (Angulo 2011), salience adaptive structuring elements (Curic et al. 2012), nonlocal patch-distance-based amoebas (Yang and Li 2015), and haze removal (Zhang and Wei 2019) [23–27]. The adaptive nature of amoeba-based filtering [22] makes it efficient in many dynamic applications, such as range imaging, medical imaging, segmentation, and image denoising. For CT images, some prior knowledge of image exists because of human body anatomy and its symmetry and contagious nature of pixel spread, which allows amoeba to extract missing information from the reconstructed image [28, 29].

In this reported work, the amoeba-based image filtering is customized for CT images acquired through filtered back projection (FBP) using sparse projection data. The proposed and customized amoeba scheme enhances the quality of the degraded sparse-view FBP reconstructed image. The amoeba kernel is derived from a pilot image based on the Wiener filter. The Wiener filter is much superior in image denoising and restoration than many other techniques, such as simple inverse filtering, Gaussian filtering, and mean filtering [30]. Therefore, the Wiener filter-based pilot image suppresses noise while preserving the image details, unlike the Gaussian-based pilot in classical amoeba and its variants [22, 26, 30]. Furthermore, the presented work also improves the methodology for amoeba shape acquisition by replacing the classical amoeba distance-based approach with region-based segmentation. The scheme is implemented using simulated and clinically reconstructed head CT phantoms. The proposed scheme is applied to noisy sparse projection data, and the reconstructed image quality is also investigated using multiple image quality metrics. Amoeba-based filtering is customized such that the image similarity index improves at even a lesser radiation dose.

The detail of the proposed research methodology and case study is given in the next section, followed by Results and Discussion, and then by Conclusion.

2. Methodology

Many modern reconstruction techniques, including advanced reconstruction techniques, use sophisticated postprocessing/image processing techniques for better representation of the reconstructed image. The dynamic and adaptive nature of Amoeba filtering makes it a strong candidate for CT application. Amoeba filtering (Lerallut et al. 2007) [22] is a particular case of spatially variant image filtering, which considers the image gradient for determining the amoeba kernel shape. The classical amoeba filtering is dependent upon the amoeba distance-based approach for the growth of amoeba [22]; this generic approach is generally efficient in most natural images. However, CT images are generally divided into various regions, based on human anatomy and test phantoms. The proposed scheme uses region-based segmentation (RBS) for amoeba shaping mechanism; hence, it is more related to the CT problem and solves it more aptly as compared to the classical amoeba.

It is noteworthy that the amoeba kernel is derived from a pilot image. Classical amoeba filters [22] and its variants predominantly use a large Gaussian filter to create the pilot image. Although the Gaussian pilot ensures significant smoothing; however, it still contains significant noise which limits the growth of the amoeba body. To offer improved enhancement of scans, a scheme comprising of Wiener filter-based pilot image and region-based segmentation (RBS) for amoeba kernel shaping is proposed.

2.1. Wiener Filter-Based Pilot Image. As the shape of the amoeba is dependent upon the center pixel of the sliding window, it is essential that the amoeba is not wrapped around a noisy pixel. As a remedy, the amoeba shape is calculated from a pilot image instead of the degraded reconstructed image. Wiener filter is very efficient in image denoising and restoration applications as it uses image degradation function and noise statistics [30]. The Wiener filter is adaptively applied to the degraded reconstructed image. The applied smoothing depends upon the image variance; the greater the variance, the lesser the smoothing or vice versa [30, 31]. Thus, the pilot image, so formed has minimal image degradation and improved edge preservation.

The Wiener filtered image (W) applied to degraded image intensity D , with all pixels $p = 1: P$, is given as

$$W(p) = \mu_L(p) + \left(\frac{\sigma_L^2(p) - \sigma_n^2}{\sigma_L^2(p)} \right) (D(p) - \mu_L(p)), \quad (1)$$

where each pixel index p is represented with $(x, y)|_{x=1:X, y=1:Y}$, σ_n^2 is the noise variance of the degraded image D , and μ_L and σ_L^2 represent the mean and variance, respectively, in a 2D sliding window about pixel p , computed using

$$\mu_L(p) = \frac{1}{UV} \sum_{u=1}^U \sum_{v=1}^V I_p(u, v), \quad (2)$$

$$\sigma_L^2(p) = \left[\frac{1}{UV} \sum_{u=1}^U \sum_{v=1}^V I_p^2(u, v) \right] - \mu_L^2(p), \quad (3)$$

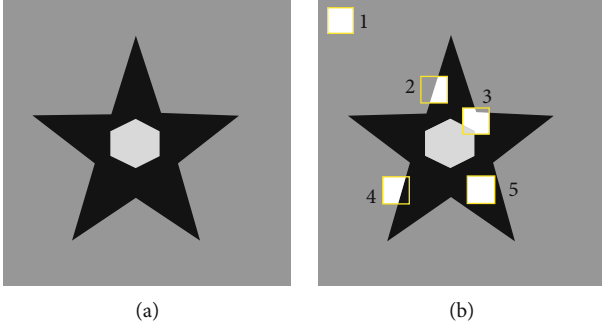


FIGURE 1: Self-shaping amoeba based on the location of sliding window. (a) Sample image. (b) Initially, square shape kernel is modified at different spatial locations within the image.

where $I_p(u, v)$ is the matrix containing intensity values within the local neighborhood about pixel $p(x, y)$, and U and V define the size of the 2D sliding window with running indices u and v .

2.2. Proposed Amoeba Filter Kernel Using RBS (Region-Based Segmentation). The proposed amoeba adapts its shape with respect to the internal image contours and edges. The amoeba filter uses the classical sliding window model for image filtering, where the window is centered at each pixel of the image. The shape of the amoeba kernel is initialized as the entire sliding window (square), which then adopts the shape based on window contents. The amoeba shaping algorithm is inspired by automated segmentation applications and techniques, such as active contours models and its variants [22, 32–34]. The proposed amoeba shaping uses region-based segmentation (RBS) through multilevel thresholding [35–38].

In the proposed amoeba shaping mechanism, a “region” is referred to a cluster of contiguous pixels, of uniform/near-uniform image intensities, inside the sliding window. The surrounding contour is automatically detected by the proposed algorithm. The amoeba shape remains square on sliding windows with little/no image intensity variation. However, with multiple variations in intensities, amoeba takes the shape of the region containing the window-center pixel. The amoeba shaping process is illustrated on a test image in Figure 1. The image contains three intensity levels. Different instances of the rectangular sliding window are represented by a (yellow) rectangle outlined in Figure 1(b), whereas the different adopted amoeba shapes in the windows are shown in white color. The two rectangular shaped amoebas 1 and 5 contain no variation. However, 2, 3, and 4 amoebas take nonrectangular shapes of the region containing center pixel.

The sliding window, $I_p(u, v)$, around the pixel $p(x, y)$ contains ‘ N ’ regions ($R_1 : R_N$) given as

$$\bigcup_{n=1}^N R_n = I_p(u, v) | R_{n1} \cap R_{n2} = \emptyset \quad \forall n1 \neq n2, \quad (4)$$

where region R_n is the n^{th} segmented region inside the sliding window $I_p(u, v)$. Image histogram (H) of $I_p(u, v)$ is

computed, and the gray levels are classified into multiple bins or clusters based on adaptive multilevel thresholding. Discontinuities, interclass variations, peaks, and valleys in the histogram are used to determine adaptive multilevel thresholds ($T_{1:N}$). Various adaptive multilevel thresholding techniques are available in the literature [39–43]. This reported work uses Otsu’s method [42, 43], which is a widely used technique in computer vision and image processing applications. Otsu’s method sets the optimal threshold levels as the values which maximize the variance between classes or bins [42, 43]. A bin of interest is determined by the threshold levels containing the intensity of the window center, $p(x, y)$. The segmented binary image mask determining the pixels included in the bin of interest (B_{in}) is given as

$$B_{in}(u, v) = \begin{cases} 1 & \text{if } T_{in-1} < I_p(u, v) \leq T_{in} \\ 0 & \text{otherwise} \end{cases} | p(x, y) \in B_{in}, \quad (5)$$

where T_{in-1} and T_{in} are the corresponding lower and upper threshold limits determining the bin of interest B_{in} . Some subregions inside B_{in} may be noncontiguous, so only a subregion containing center pixel is used in final amoeba shape formation. This is manifested using connected components labeling, a common technique in image processing and computer vision applications for labeling and extracting image disjoints [30, 44, 45]. Details along with the algorithm representation and pseudocode are given in appendix A and B, respectively.

The final amoeba kernel shape, $A(u, v)$, is constituted of the pixels making up the central subregion containing the central pixel $p(x, y)$ in the sliding window or local neighborhood (U, V). The same process is repeated for each sliding to find the corresponding amoeba kernel shapes. Mean operation is then applied on each final amoeba kernel shape to compute the intensity of the output image at the corresponding central pixel.

The effectiveness of the proposed self-shaping amoeba filter kernel in computed tomography applications is showcased in Figures 2(a)–2(d) using the Shepp-Logan CT phantom (512×512 pixels). Four different instances of shapes adapted by the amoeba depending upon the spatial location of the sliding window are displayed in each of rows (a) to (d) of Figure 2. Column 1 in each row (Figures 2(a)–2(d)) demonstrates the location of the sliding window in the image; column 2 displays the zoomed contents of the sliding window. White regions in column 3 are representing the adapted amoeba filter kernel shapes. Figure 2 uses a sliding window of 50×50 pixels for better visualization of amoeba shaping.

2.3. Amoeba Filtering-Based CT Image Enhancement. The most basic and common head CT phantom, Shepp-Logan, was used in this implementation as the subject to acquire the projection data. It is a standard test image and synthetic phantom. The size of the head phantom was kept as 512×512 pixels, as shown in Figure 3(a). Ninety fan-beam projections were taken from view angles 0 to 180 degrees; with an angular sampling interval of 2 degrees. The detector sensors were spaced at 0.25 mm.

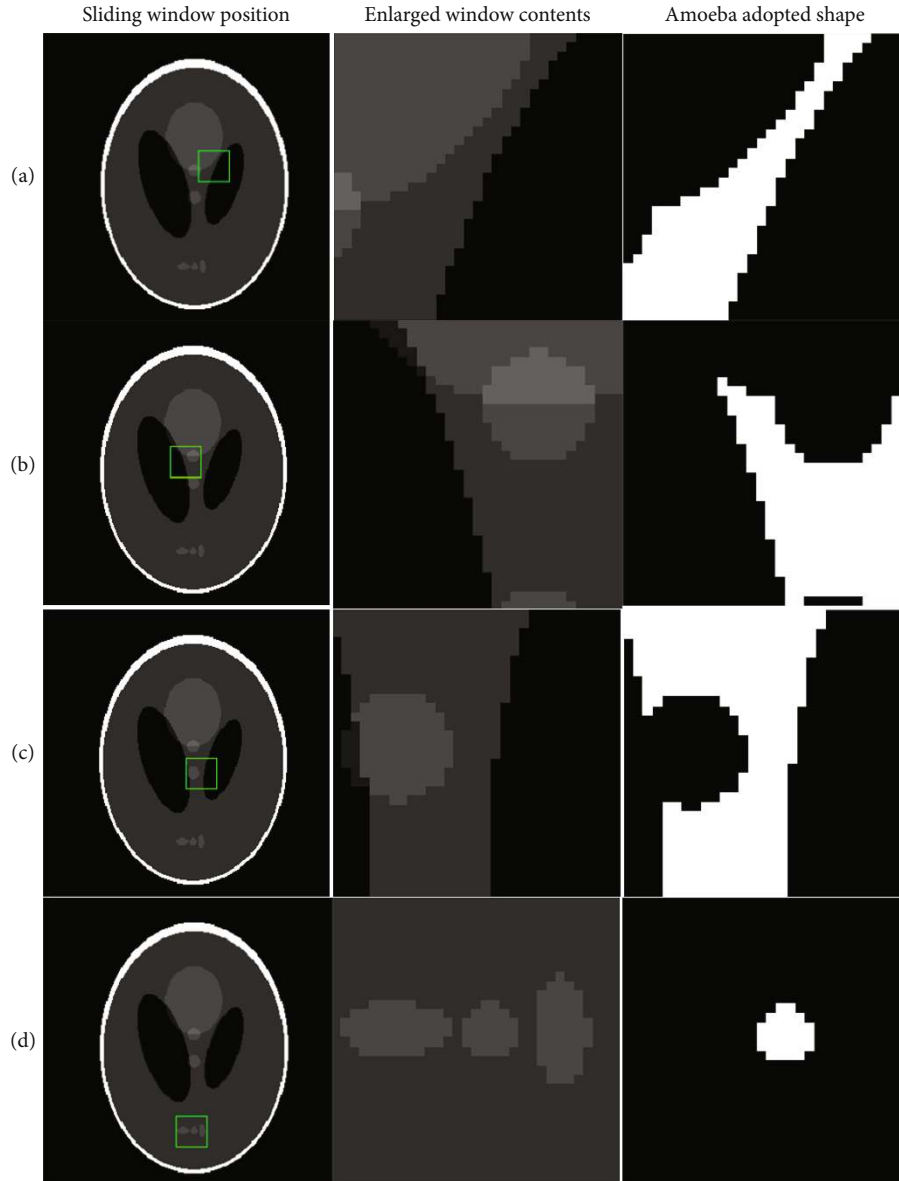


FIGURE 2: Adopted amoeba kernel shape at various spatial location of sliding window. Each row (a–d) contains a sample of sliding window at a spatial location, along with an enlarged view of the window content and the adopted amoeba shape.

The acquired projection data contains noise from numerous factors including photons, quantization, and electronics. In the literature, various medical imaging techniques use different types of noise models in which the Gaussian model is commonly used for CT [46–49]. Therefore, in the proposed work, additive white Gaussian noise (AWGN) at 3 dB SNR level is used. Filtered back projection (FBP) reconstruction algorithm is then applied to the projection data, which is the most commonly used CT reconstruction algorithm [8, 50, 51]. The resultant FBP reconstructed image is of low quality and is severely degraded (due to reduced dose), as shown in Figure 3(b).

The smoothness of the reconstructed image was lost due to undersampled FBP reconstruction. The amoeba filtering was used for smoothening without compromising on edge details. The size of the sliding window was kept as 9×9 pixels

for the pilot image and amoeba shaping, through the mechanism described in the previous section. Once the amoeba shape is determined, the mean filtering was applied.

The proposed amoeba denoising scheme was also implemented to clinically reconstructed CT head image from Phillips CT healthcare case study, available at [52] as shown in Figure 4. The size of the reconstructed head phantom was kept at 512×512 pixels. The sparse-view projections were acquired at an angular sampling of 2 degrees, with AWGN added in projections at 3 dB SNR. The pilot image for amoeba shaping was acquired using a Wiener filter with a kernel neighborhood of size 9×9 pixels.

2.4. Image Quality Metrics. The quality of the scheme was evaluated using multiple full-reference objective image quality metrics [53]. The image quality metrics use the

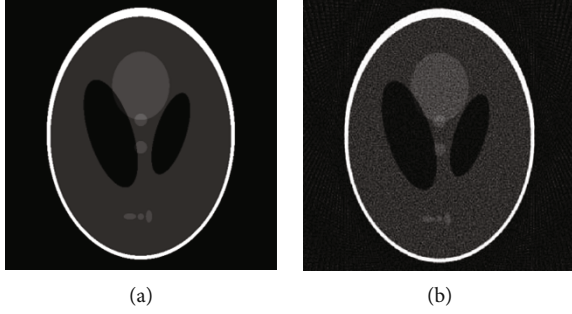


FIGURE 3: Sparse-view FBP reconstruction of simulated phantom (a) Shepp-Logan phantom. (b) 2-degree angularly sampled FBP reconstruction of (a).

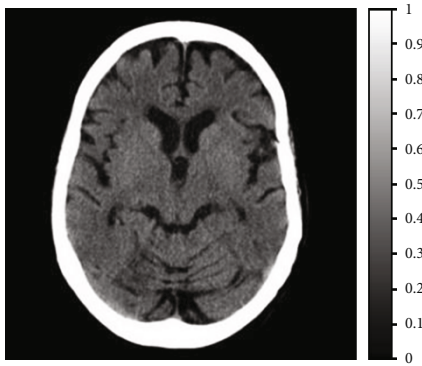


FIGURE 4: Clinically reconstructed head CT phantom acquired from Phillips CT healthcare case study, available at [52].

distortion-free original image/phantom as a reference. The image quality metrics include RMSE (root mean square error), PSNR (peak-signal-to-noise ratio), SSIM (structural similarity index metric), EPI (edge preservation index), SI (sharpness index), SC (structural content), and NAE (normalized absolute error).

RMSE is computed by taking the square root of the average of squares of the differences of the corresponding pixels in the test and reference images and is given as

$$\text{RMSE} = \sqrt{\frac{1}{mn} \sum_{i=0}^{m-1} \sum_{j=0}^{n-1} [A(i, j) - B(i, j)]^2}, \quad (6)$$

where A is the reference image, B is a test image, and m and n define the size of the reference and test images.

The PSNR is expressed in terms of decibels (dB), calculated as

$$\text{PSNR} = 20 \log_{10} \left(\frac{I_{\max}}{\text{RMSE}} \right), \quad (7)$$

where I_{\max} is the maximum pixel intensity value in the image.

PSNR and RMSE use pixel intensity differences to evaluate the image quality, which although have clear mathematical and physical significance but offer very less in terms of

human visual perception of image quality [53, 54], whereas SSIM incorporates the luminance, contrast, and structural details and similarity of the compared images, giving much appropriate representation of the human preserved visual image quality [53, 54]. These terms, namely, the luminance index (li), the contrast index (ci) and the structural index (si); combines to determine the SSIM value as

$$\text{SSIM}_{(x,y)} = [\text{li}_{(x,y)}]^\alpha \cdot [\text{ci}_{(x,y)}]^\beta \cdot [\text{si}_{(x,y)}]^\gamma, \quad (8)$$

where

$$\text{li}_{(x,y)} = \frac{2\mu_x\mu_y + C_1}{\mu_x^2 + \mu_y^2 + C_1}, \quad (9)$$

$$\text{ci}_{(x,y)} = \frac{2\sigma_x\sigma_y + C_2}{\sigma_x^2 + \sigma_y^2 + C_2}, \quad (10)$$

$$\text{si}_{(x,y)} = \frac{\sigma_{xy} + C_3}{\sigma_x\sigma_y + C_3}, \quad (11)$$

where μ_x and μ_y are intensity means along the x and y directions, σ_x and σ_y are image standard deviations, and σ_{xy} is the cross-covariance of images in x and y directions [53]. C_1 , C_2 , and C_3 are small constant terms added to avoid instability [53]. α , β , and γ are positively valued parameters used to adjust the importance of three corresponding factors. For simplification, α , β , and γ are kept as unity, and by default, C_3 is kept as half of C_2 [53]. The simplified SSIM index is thus expressed as

$$\text{SSIM}_{(x,y)} = \frac{(2\mu_x\mu_y + C_1)(2\sigma_x\sigma_y + C_2)}{(\mu_x^2 + \mu_y^2 + C_1)(\sigma_x^2 + \sigma_y^2 + C_2)}. \quad (12)$$

The edge preservation index (EPI) indicates the amount of edges that are preserved in the test image [55, 56]. Edges are of great importance in medical imaging as they contain significant information such as tumor or lesion contour identification [55, 56]. The EPI between reference image A and test image B is determined as

$$\text{EPI}(A, B) = \frac{\sum(\Delta A - \mu_{\Delta A})(\Delta B - \mu_{\Delta B})}{\sqrt{\sum(\Delta A - \mu_{\Delta A})^2(\Delta B - \mu_{\Delta B})^2}}, \quad (13)$$

where ΔA and ΔB are obtained from filtering A and B using a high-pass filter [55, 56], such as a simple 3×3 Laplacian operator-based spatial domain filter H given as

$$H_{xy} = \left\{ \begin{array}{l} 1, \text{ for } x, y = 1, 2, 3 \text{ and } x, y \neq 2 \\ - \sum_{i,j=1}^3 H_{xy} \text{ for } x = y = 2 \end{array} \right\}. \quad (14)$$

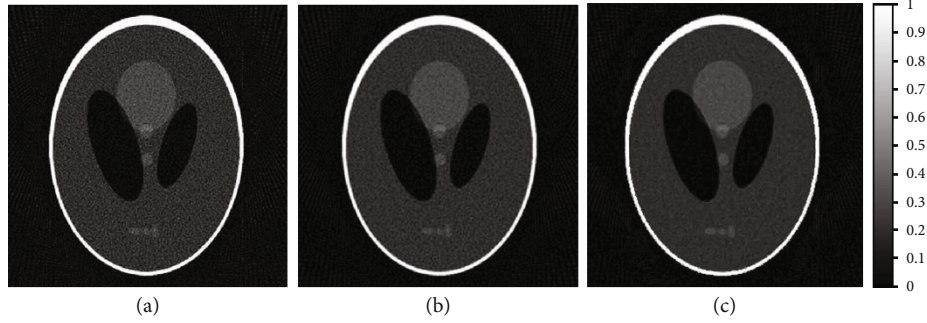


FIGURE 5: Comparison of sparse-view FBP reconstructed image with proposed RBS amoeba and classical amoeba schemes, using Gaussian filtering-based pilot image. (a) 2-degree angular sampling-based sparse-view FBP reconstruction. (b) Classical amoeba distance-based image denoising of sparse-view FBP. (c) Proposed RBS amoeba-based denoising using Gaussian-filtered pilot image.

TABLE 1: Image quality comparison of proposed and classical shaping mechanisms.

Scheme name	RMSE	PSNR (dB)	SSIM	EPI	SI	SC	NAE
Sparse-view FBP	0.074	22.61	0.24	0.211	121	0.988	0.428
Amoeba distance (with Gaussian pilot)	0.059	24.56	0.42	0.253	332.8	0.990	0.286
RBS amoeba shaping (with Gaussian pilot)	0.059	24.51	0.52	0.261	1683.9	1.008	0.235

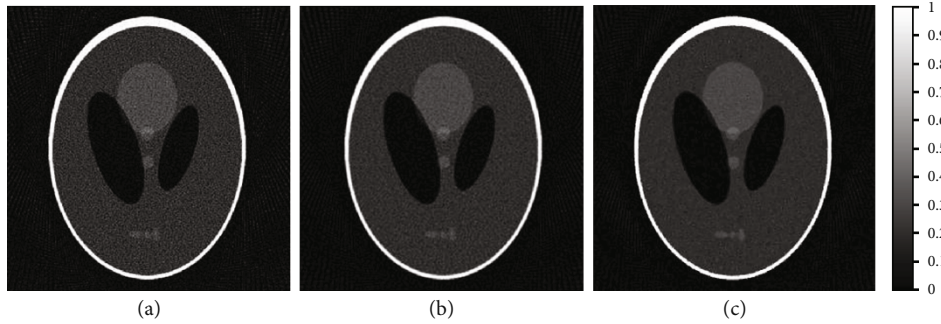


FIGURE 6: Comparison of sparse-view FBP reconstructed image with classical and proposed amoeba schemes. (a) 2-degree angular sampling-based sparse-view FBP reconstruction. (b) Classical amoeba filtering-based image denoising of (a). (c) Proposed scheme with RBS amoeba denoising of (a) using Wiener pilot image.

$\mu_{\Delta A}$ and $\mu_{\Delta B}$ represent the mean of ΔA and ΔB , respectively. The EPI values range between 0 and 1; the higher the value the better is the image quality [55, 56].

Sharpness index (SI) is a no-reference image quality metric based on the image Fourier phase spectrum, which contains important information such as image geometry and contour details [55, 57]. The sharpness index (SI) of a test image B is defined as

$$SI = -\log_{10} \mathcal{O} \left(\frac{\mu - TV(B)}{\sigma} \right), \quad (15)$$

where $TV(B)$ refers to the total variation of image B , $\mu = E(TV(B))$, $\sigma^2 = \text{Var}(TV(B))$, and \mathcal{O} is the tail of the Gauss distribution [55, 57]. A higher SI value corresponds to better image quality.

Structural content (SC) is a full-reference image quality metric based on image structural similarity and spatial arrangement of pixels in an image [58, 59]. The structural

content metric equals 1 when two same images are compared. Structural content for reference image A and test image B is determined as

$$SC(A, B) = \frac{\sum_{x=1}^X \sum_{y=1}^Y [A(x, y)]^2}{\sum_{x=0}^X \sum_{y=0}^Y [B(x, y)]^2}. \quad (16)$$

Normalized absolute error (NAE) is a full-reference image quality metric measuring the statistical difference between the reference and test images [58, 60]. A lower NAE value corresponds to better image quality. NAE for reference image A and test image B is given as

$$NAE = \frac{\sum_{x=1}^X \sum_{y=1}^Y (|A(x, y) - B(x, y)|)}{\sum_{x=1}^X \sum_{y=1}^Y (|A(x, y)|)}. \quad (17)$$

TABLE 2: Image quality comparison of the proposed Wiener filtering-based RBS amoeba scheme with the classical amoeba filtering scheme.

Scheme name	RMSE	PSNR	SSIM	EPI	SI	SC	NAE
Sparse-view FBP	0.074	22.61	0.24	0.211	121	0.988	0.428
Classical amoeba	0.059	24.56	0.42	0.253	332.8	0.990	0.286
Proposed RBS amoeba	0.052	25.56	0.58	0.376	1739.8	1.002	0.233

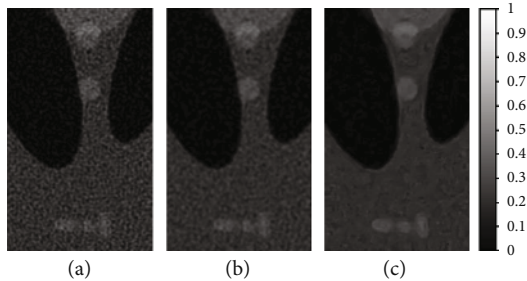


FIGURE 7: Comparison of enlarged ROI in sparse-view FBP reconstruction image with proposed amoeba and classical amoeba schemes. (a) 2-degree angular sampling-based sparse-view FBP reconstruction. (b) Classical amoeba distance-based image denoising of (a). (c) Proposed RBS amoeba denoising of (a) using Wiener pilot.

3. Results and Discussion

3.1. Shepp-Logan Phantom-Based Sparse-View FBP Implementation

3.1.1. Experiment 1: Comparison of Proposed and Classical Shaping Mechanisms. To investigate the efficacy of the proposed RBS amoeba shaping mechanism, the proposed scheme is compared with the existing classical amoeba distance-based shaping. The two schemes are compared using Shepp-Logan-based sparse projections and a pilot image obtained from the Gaussian filtering. Mean filtering is then applied to the acquired amoeba shapes/kernels and evaluated based on the abovementioned image quality metrics, as shown in Figure 5.

The comparison of sparse-view FBP image with classical amoeba and proposed RBS amoeba schemes are shown in Figure 5. The sparse-view FBP reconstructed image is shown in Figure 5(a). The classical amoeba improves the image quality as shown in Figure 5(b). The RBS-based amoeba denoising with the Gaussian filter-based pilot is shown in Figure 5(c).

The proposed RBS amoeba shaping is visually better as compared to the classical amoeba scheme, with better SSIM, EPI, SI, SC, and NAE values, while presenting very similar quality in terms of PSNR and RMSE, as seen in Table 1.

3.1.2. Experiment 2: Comparison of Proposed Wiener Filtering-Based RBS Amoeba Scheme with Classical Amoeba Scheme. The proposed scheme, RBS amoeba with Wiener pilot, is compared with the classical amoeba scheme (Gaussian pilot), as shown in Figure 6. The 2-degree angular sampling-based FBP is shown in Figure 6(a). The classical amoeba-based enhanced image is shown in Figure 6(b), while

the proposed amoeba scheme-based denoised image is shown in Figure 6(c). Table 2 depicts that the proposed scheme presents superior results as compared to the classical amoeba scheme, using various image quality metrics.

For better visualization and focused analysis of this comparison, Figure 7 presents an enlarged version of the results shown in Figure 6. The region of interest (ROI) is focused inside the phantom, such that the comparison does not include the streak artifacts outside the phantom (skull) boundary. The image quality is compared for the enlarged ROI only. The enlarged ROI of the FBP reconstructed image is shown in Figure 7(a), with the classical and proposed amoeba schemes shown in Figures 7(b) and 6(c), respectively. The proposed scheme is visually and statistically better than the classical amoeba scheme, as shown in Table 3. The focused ROI analysis demonstrates that the edges are more pronounced with enhanced contrast in the proposed scheme denoising, with better smoothing and noise suppression.

3.2. Real Clinical Head CT-Based Implementation. The comparison of sparse-view FBP reconstruction of clinically reconstructed CT image, available at [52], with the classical and proposed amoeba denoising schemes, is shown in Figure 8. The sparse-view FBP reconstruction is shown in Figure 8(a). The classical amoeba (Gaussian pilot and amoeba distance) is shown in Figure 8(b), while the proposed scheme denoising is shown in Figure 8(c).

The proposed RBS amoeba shaping outperforms the classical amoeba scheme in terms of various image quality metrics, as shown in Table 4.

3.3. Robustness Comparison. The robustness of the scheme was also tested by analyzing the image quality at various projection noise levels. Shepp-Logan phantom of size 512×512 was used for projection acquisition at 2-degree angular intervals. The FBP reconstruction quality was compared with classical amoeba and proposed Wiener pilot-based RBS amoeba denoising. The comparison demonstrates that the scheme is robust in the presence of noise, with both increased similarity index and lower error floors, as depicted in Figures 9 and 10, respectively.

3.4. Comparison of Schemes at Various Projection View Sampling. The effectiveness of the scheme was also evaluated by analyzing the image quality at various projection view sampling. Shepp-Logan phantom of size 512×512 was used for FBP reconstruction, while the projection sampling ranges from 8-degree incremental angles to 0.5 degrees. The quality was compared with classical amoeba and proposed Wiener pilot-based RBS amoeba denoising. The comparison

TABLE 3: Image quality comparison of schemes using enlarged ROI images.

Scheme name	RMSE	PSNR	SSIM	EPI	SI	SC	NAE
Sparse-view FBP	0.048	26.28	0.32	0.266	0.48	0.936	0.300
Classical amoeba	0.030	30.23	0.54	0.410	1.50	0.987	0.185
Proposed RBS amoeba	0.024	32.23	0.68	0.423	32.70	1.000	0.131

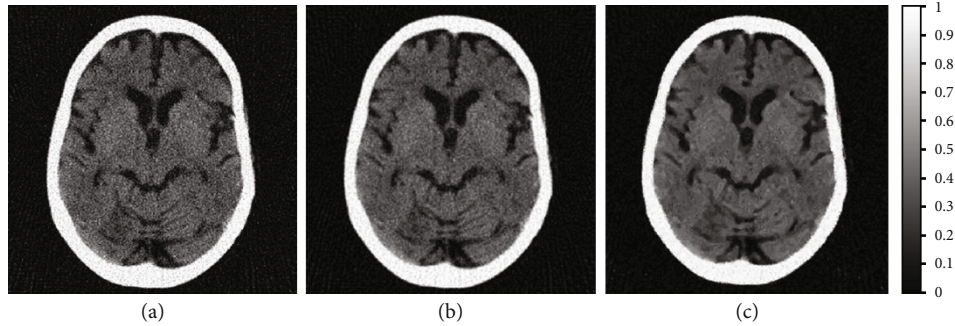


FIGURE 8: Comparison of sparse-view FBP reconstructed image with classical and proposed amoeba schemes, applied on clinically reconstructed CT image. (a) 2-degree angular sampling-based sparse-view FBP reconstruction. (b) Classical amoeba filtering-based image denoising of (a). (c) Proposed scheme with RBS amoeba denoising of (a) using Wiener pilot image.

TABLE 4: Image quality comparison of the proposed and classical schemes in real clinical head CT-based implementation.

Scheme name	RMSE	PSNR	SSIM	EPI	SI	SC	NAE
Sparse-view FBP	0.085	21.32	0.22	0.211	5.75	0.959	0.290
Classical amoeba	0.053	25.46	0.37	0.210	40.17	0.993	0.179
Proposed RBS amoeba	0.047	26.52	0.44	0.289	350.3	1.002	0.142

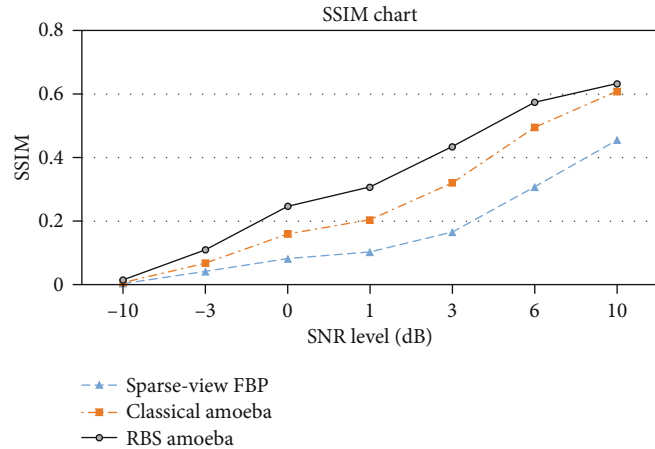


FIGURE 9: Robustness comparison of sparse-view FBP reconstruction with classical and proposed amoeba schemes, SSIM performance of the schemes at various noise levels in projection data.

demonstrates that the scheme performs better even with a lesser number of projection views, as shown in Figure 11. Hence, the scheme presents an alternate radiation dose reduction method through the enhancement of sparse-view.

4. Discussion

The results demonstrate that the proposed RBS amoeba scheme has improved results as compared to the classical

amoeba scheme. The sparseness in projections results in missing data; however, the human anatomy with symmetric and naturally contiguous pixels serves as prior knowledge and enables the proposed scheme to perform better in this scenario. Therefore, the proposed scheme is a more suitable candidate for CT images. Moreover, the RBS scheme provides better contrast as compared to the classical amoeba distance-based denoising, as shown in enlarged ROI-based comparison.

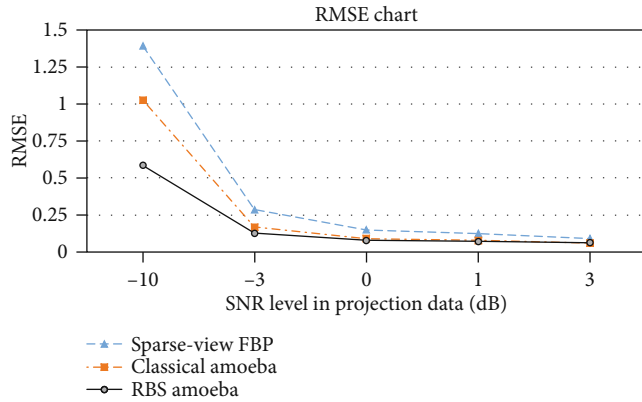


FIGURE 10: Robustness comparison of sparse-view FBP reconstruction with classical and proposed amoeba schemes, on the basis of RMSE performance of the schemes at various noise levels in projection data.

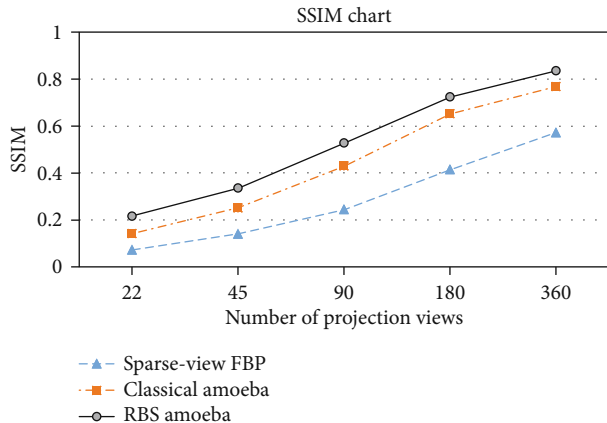


FIGURE 11: Comparison of sparse-view FBP reconstruction with classical and proposed amoeba schemes, SSIM performance of the schemes using FBP reconstructions at various projection view sampling.

The proposed scheme is more robust and performs significantly better than the classical amoeba filtering in the presence of projection noise. The scheme inherits significant image noise reduction, Gaussian, and otherwise, due to dependence on Wiener and Amoeba filtering [22, 26, 30]. The superiority of Wiener filter pilot over Gaussian filter pilot corresponds to lesser error floor in case of increased noise levels; while the similarity is increased mainly because of the region-based approach of the scheme matching the human anatomy. The proposed scheme provides better smoothing of the degraded image without intervening in the contour boundaries. The scheme provides an alternate method to reduce the radiation dose involved in CT, through enhancement of FBP reconstruction from a lesser number of projection views to a quality equivalent to more view data.

A limitation of the proposed scheme is its dependency on Otsu's multilevel thresholding method which makes it computational expensive and, therefore, is not appropriate

for real-time applications. However, this can be mitigated by the use of advanced and high-speed processors, such as GP-GPU (general purpose graphical processor units), as the scheme has potential to run in parallel. Therefore, the future research directions may include scheme optimization for real-time applications and implementation on GP-GPU. Moreover, the adaptive nature of the proposed amoeba-based filtering indicates scheme implementation in many dynamic applications is worth investigating, signifying future application of the scheme on denoising of natural images, industrial-CT, and nondestructive testing (NDT) data.

5. Conclusion

This paper presents an efficient and novel postprocessing scheme for CT radiation dose reduction and enhancement of FBP reconstructed image from sparse-view noisy CT scans. In this work, a new type of amoeba filtering is presented, which is customized for CT images. Region-based segmentation (RBS) using multilevel thresholding was used in the amoeba kernel shaping, which is more effective in medical imaging applications as it is similar to the symmetric and region-based nature of the human body anatomy. The pilot image uses Wiener filter, which helps in noise suppression while keeping the edge and contour details required for amoeba shaping. The scheme is supported by computer simulations using fan-beam projections of clinically reconstructed and simulated head CT phantoms. The results demonstrate that the proposed Wiener filter-based RBS amoeba scheme is visually and statistically better than classical amoeba filtering for CT image, as evaluated using various image quality matrices. The presented scheme is more robust to noise in CT projections and effective for enhancing few-view reconstruction. In the future, the implementation of the scheme on more medical as well as industrial phantoms will be undertaken. The introduction of the Wiener filter-based RBS amoeba scheme makes way for a family of morphological, median, and other filters based on the presented framework. The algorithm has the potential to run in parallel; thus, implementation of the proposed scheme on GP-GPU will also be a possible future avenue.

Appendix

A. Pseudoalgorithm for Connected Component Labeling

The pseudo algorithm to scan and segment connected regions is given below:

B. Pseudocode for Connected Component Labeling

Pseudocode to scan and segment connected regions, using 4-connected component mask, is given below:

- On the first pass:
1. Raster scan the sliding window (iteratively scan pixels by one row at a time)
 2. If the pixel is not the background (i.e., 0)
 - i. Get the neighboring pixels of the current pixel
 - ii. If there are no neighbors, uniquely label the current pixel and continue
 3. Otherwise, label the current pixel with the smallest neighbor label
 4. Store the equivalence between neighboring labels (if neighbors have different labels)
- On the second pass:
5. Raster scan the sliding window (iteratively scan pixels by one row at a time)
 6. If the pixel is not the background (0)
 - i. Relabel the pixel with the lowest equivalent label

PSEUDOCODE 1:

```

LabelCount = 0 ; //Initialize Label counter.
EquivalenceTable = [] ; //Initialize equivalence table of labels
For u = 1:U ; //Raster scan the window (iteratively scan one row at a time)
  For v = 1:V ; //iteratively scan pixels in each column of the selected row
    If Ip(u,v) ≠ 0 ; //If the pixel is NOT background (i.e., 0)
      Neighbors = [Label(u,v-1), Label(u-1,v)]; //Get neighbor labels (one pixel above, and one on left/prior)
      ; //Note: neighbors for 8-connected mask include pixels to the
      ; //top-right, top, top-left and left of the pixel(u,v)
      If Neighbors = [ ] ; //If no neighbor pixel is labeled
        Label(u,v) = LabelCount + 1 ; //uniquely label the pixel
        LabelCount = LabelCount + 1 ; //increment label counter
      End If
    Else Label(u,v) = min (Neighbors) ; label the current pixel as the neighbor with the smallest label
      If [length(Neighbors) = 2] && [Neighbors(1) ≠ Neighbors(2)]
        EquivalenceTable = [EquivalenceTable, ((min(Neighbors), max(Neighbors)))]
      ; //Record equivalencies of neighbor labels (Mx2 matrix)
      End If
    End If
  End For
  Neighbors = [ ] ; //Reset neighbor pointer.
End For
End For
; Second Pass: Relabeling equivalencies
Sort (EquivalenceTable, 1) ; //Sort the Equivalence Table based on first column
EqualityCount = rows(EquivalenceTable) ; //Total equivalencies = number of rows in Table
Do
  L1 = EquivalenceTable (EqualityCount,1) ; //Smaller label in selected Equivalence Table entry
  L2 = EquivalenceTable (EqualityCount,2) ; //Larger label in selected Equivalence Table entry
  Labels(find(Labels == L2)) = L1 ; //Relabel all instances of larger label with smaller label
  EqualityCount = EqualityCount - 1 ; //Decrement to target next equivalency
While EqualityCount >= 1

```

PSEUDOCODE 2:

Data Availability

No data were used to support this study.

Conflicts of Interest

The authors declare that there is no conflict of interest regarding the publication of this paper.

References

- [1] J. C. Hutchinson, S. C. Shelmerdine, I. C. Simcock, N. J. Sebire, and O. J. Arthurs, "Early clinical applications for imaging at microscopic detail: microfocus computed tomography (micro-CT)," *British journal of radiology*, vol. 90, no. 1075, p. 20170113, 2017.
- [2] E. Seeram, *Digital Radiography: Physical Principles and Quality Control*, Springer, 2019.
- [3] B. B. Nelson, C. E. Kawcak, M. F. Barrett, C. W. McIlwraith, M. W. Grinstaff, and L. R. Goodrich, "Recent advances in articular cartilage evaluation using computed tomography and magnetic resonance imaging," *Equine veterinary journal*, vol. 50, no. 5, pp. 564–579, 2018.
- [4] F. Smith-Jack and R. Davies, "Cone beam computed tomography: an update for general dental practitioners," *Dental Update*, vol. 45, no. 4, pp. 329–338, 2018.

- [5] B. Preim and C. P. Botha, *Visual Computing for Medicine: Theory, Algorithms, and Applications*, Newnes, 2013.
- [6] L. Axel, P. H. Arger, and R. A. Zimmerman, "Applications of computerized tomography to diagnostic radiology," *Proceedings of the IEEE*, vol. 71, no. 3, pp. 293–297, 1983.
- [7] D. J. Brenner and E. J. Hall, "Computed Tomography and radiation exposure," *New England Journal of Medicine*, vol. 358, no. 8, pp. 850–853, 2008.
- [8] J. Hsieh, *Computed tomography: principles, design, artifacts, and recent advances*, SPIE, Bellingham, WA, 2009.
- [9] H. Zhang, J. Ma, J. Wang, Y. Liu, H. Lu, and Z. Liang, "Statistical image reconstruction for low-dose CT using nonlocal means-based regularization," *Computerized Medical Imaging and Graphics*, vol. 38, no. 6, pp. 423–435, 2014.
- [10] S. A. Melli, K. A. Wahid, P. Babyn, D. M. Cooper, and A. M. Hasan, "A wavelet gradient sparsity based algorithm for reconstruction of reduced-view tomography datasets obtained with a monochromatic synchrotron-based X-ray source," *Computerized Medical Imaging and Graphics*, vol. 69, pp. 69–81, 2018.
- [11] Y. Liu, H. Shangguan, Q. Zhang, H. Zhu, H. Shu, and Z. Gui, "Median prior constrained TV algorithm for sparse-view low-dose CT reconstruction," *Computers in Biology and Medicine*, vol. 60, pp. 117–131, 2015.
- [12] Y. Ohno, H. Koyama, S. Seki, Y. Kishida, and T. Yoshikawa, "Radiation dose reduction techniques for chest CT: principles and clinical results," *European Journal of Radiology*, vol. 111, pp. 93–103, 2019.
- [13] X. Wang, G. Hu, B. Yan, Y. Han, L. Li, and S. Bao, "Fast low-dose reconstruction from truncated data in dental CT," *IEEE Transactions on Nuclear Science*, vol. 60, no. 1, pp. 174–181, 2013.
- [14] J. Wang, S. Wang, L. Li, Y. Fan, H. Lu, and Z. Liang, "Virtual colonoscopy screening with ultra low-dose CT and less-stressful bowel preparation: a computer simulation study," *IEEE Transactions on Nuclear Science*, vol. 55, no. 5, pp. 2566–2575, 2008.
- [15] E. Sidky, C. Kao, and X. Pan, "Accurate image reconstruction from few-views and limited-angle data in divergent-beam CT," *Journal of X-Ray Science and Technology*, vol. 14, no. 2, pp. 119–139, 2006.
- [16] W. Cong, H. Shan, X. Zhang, S. Liu, R. Ning, and G. Wang, "Deep-learning-based breast CT for radiation dose reduction," *Developments in X-Ray Tomography XII*, vol. 11113, 2019.
- [17] H. Kudo, T. Suzuki, and E. A. Rashed, "Image reconstruction for sparse-view CT and interior CT-introduction to compressed sensing and differentiated backprojection," *Quantitative Imaging in Medicine and Surgery*, vol. 3, no. 3, pp. 147–161, 2013.
- [18] C. Rampinelli, D. Origgi, and M. Bellomi, "Low-dose CT: technique, reading methods and image interpretation," *Cancer Imaging*, vol. 12, pp. 548–556, 2013.
- [19] M. Bertram, J. Wiegert, D. Schafer, T. Aach, and G. Rose, "Directional view interpolation for compensation of sparse angular sampling in cone-beam CT," *IEEE Transactions on Medical Imaging*, vol. 28, no. 7, pp. 1011–1022, 2009.
- [20] P. Lekeaka-Takunju, T. Khan, G. Harmon, S. Udpa, and L. Udpa, "X-ray tomographic inspection of nuclear fuel rods using a limited number of projections," *Materials Evaluation*, vol. 69, no. 4, pp. 495–500, 2011.
- [21] P. Lekeaka-Takunju, T. Khan, C. Bardel et al., "Assessment of nuclear fuel pellets using X-ray tomography," *International Journal of Applied Electromagnetics and Mechanics*, vol. 33, no. 3-4, pp. 1267–1272, 2010.
- [22] R. Lerallut, É. Decencière, and F. Meyer, "Image filtering using morphological amoebas," *Image and Vision Computing*, vol. 25, no. 4, pp. 395–404, 2007.
- [23] J. Debayle and J. C. Pinoli, "Spatially adaptive morphological image filtering using intrinsic structuring elements," *Image Analysis & Stereology*, vol. 24, no. 3, pp. 145–158, 2005.
- [24] J. Angulo, "Morphological bilateral filtering and spatially-variant adaptive structuring functions," *Mathematical Morphology and Its Applications to Image and Signal Processing*, vol. 6671, pp. 212–223, 2011.
- [25] V. Curic, C. L. Luengo Hendriks, and G. Borgefors, "Salience adaptive structuring elements," *IEEE Journal of Selected Topics in Signal Processing*, vol. 6, no. 7, pp. 809–819, 2012.
- [26] S. Yang and J. X. Li, "Spatial-variant morphological filters with nonlocal-patch-distance-based amoeba kernel for image denoising," *Image Analysis & Stereology*, vol. 34, no. 1, pp. 63–72, 2015.
- [27] B. Zhang and J. Wei, "Hardware implementation for haze removal with adaptive filtering," *IEEE Access*, vol. 7, pp. 142498–142506, 2019.
- [28] J. J. Cerrolaza, M. L. Picazo, L. Humbert et al., "Computational anatomy for multi-organ analysis in medical imaging: a review," *Medical Image Analysis*, vol. 56, pp. 44–67, 2019.
- [29] T. Schwarz, T. Heimann, D. Lossnitzer et al., "Multiobject segmentation using coupled shape space models," *Medical Imaging 2010: Image Processing*, vol. 7623, 2010.
- [30] R. C. Gonzalez and R. E. Woods, *Digital Image Processing*, Prentice Hall, Upper Saddle River, NJ, 3 edition, 2008.
- [31] J. S. Lim, *Two-Dimensional Signal and Image Processing*, Prentice-Hall international editions, 548 pages, Englewood Cliffs, NJ, Prentice Hall, 1990.
- [32] M. Kass, A. Witkin, and D. Terzopoulos, "Snakes: active contour models," *International Journal of Computer Vision*, vol. 1, no. 4, pp. 321–331, 1988.
- [33] T. McInerney and D. Terzopoulos, "Deformable models in medical image analysis," *Proceedings of the Workshop on Mathematical Methods in Biomedical Image Analysis*, pp. 171–180, 1996.
- [34] L. Farhi, A. Yusuf, and R. H. Raza, "Adaptive stochastic segmentation via energy-convergence for brain tumor in MR images," *Journal of Visual Communication and Image Representation*, vol. 46, pp. 303–311, 2017.
- [35] S. Pare, A. Kumar, G. K. Singh, and V. Bajaj, "Image segmentation using multilevel thresholding: a research review," *Iranian Journal of Science and Technology, Transactions of Electrical Engineering*, vol. 44, no. 1, pp. 1–29, 2020.
- [36] N. Sri Madhava Raja, V. Rajinikanth, and K. Latha, "Otsu based optimal multilevel image thresholding using firefly algorithm," *Modelling and Simulation in Engineering*, vol. 2014, 17 pages, 2014.
- [37] A. K. M. Khairuzzaman and S. Chaudhury, "Multilevel thresholding using grey wolf optimizer for image segmentation," *Expert Systems with Applications*, vol. 86, pp. 64–76, 2017.
- [38] Y. Huang and S. Wang, "Multilevel thresholding methods for image segmentation with Otsu based on QPSO," *IEEE Congress on Image and Signal Processing*, vol. 3, pp. 701–705, 2008.
- [39] S. Pare, A. K. Bhandari, A. Kumar, and G. K. Singh, "An optimal color image multilevel thresholding technique using grey-

- level co-occurrence matrix,” *Expert Systems with Applications*, vol. 87, pp. 335–362, 2017.
- [40] S. Arora, J. Acharya, A. Verma, and P. K. Panigrahi, “Multi-level thresholding for image segmentation through a fast statistical recursive algorithm,” *Pattern Recognition Letters*, vol. 29, no. 2, pp. 119–125, 2008.
- [41] M. M. Dehshibi, M. Sourizaei, M. Fazlali, O. Talaee, H. Samadyar, and J. Shanbehzadeh, “A hybrid bio-inspired learning algorithm for image segmentation using multilevel thresholding,” *Multimedia Tools and Applications*, vol. 76, no. 14, pp. 15951–15986, 2017.
- [42] N. Otsu, “A threshold selection method from gray-level histograms,” *IEEE Transactions on Systems, Man, and Cybernetics*, vol. 9, no. 1, pp. 62–66, 1979.
- [43] M. H. Merzban and M. Elbayoumi, “Efficient solution of Otsu multilevel image thresholding: a comparative study,” *Expert Systems with Applications*, vol. 116, pp. 299–309, 2019.
- [44] R. M. Haralick and L. G. Linda, *Computer and Robot Vision*, Addison-Wesley, Volume I, 1992.
- [45] L. He, X. Ren, Q. Gao, X. Zhao, B. Yao, and Y. Chao, “The connected-component labeling problem: a review of state-of-the-art algorithms,” *Pattern Recognition*, vol. 70, pp. 25–43, 2017.
- [46] P. Gravel, G. Beaudoin, and J. A. DeGuise, “A method for modeling noise in medical images,” *IEEE Transactions on Medical Imaging*, vol. 23, no. 10, pp. 1221–1232, 2004.
- [47] H. Lu, X. Li, I. T. Hsiao, and Z. Liang, “Analytical noise treatment for low-dose CT projection data by penalized weighted least-squares smoothing in the K-L domain,” *Medical Imaging 2002: Physics of Medical Imaging*, vol. 4682, pp. 146–152, 2002.
- [48] H. Gudbjartsson and S. Patz, “The rician distribution of noisy MRI data,” *Magnetic Resonance in Medicine*, vol. 34, no. 6, pp. 910–914, 1995.
- [49] T. Lei and W. Sewchand, “Statistical approach to X-ray CT imaging and its applications in image analysis. I. Statistical analysis of X-ray CT imaging,” *IEEE Transactions on Medical Imaging*, vol. 11, no. 1, pp. 53–61, 1992.
- [50] X. Pan, E. Y. Sidky, and M. Vannier, “Why do commercial CT scanners still employ traditional filtered back-projection for image reconstruction?,” *Inverse Problems*, vol. 25, no. 12, p. 123009, 2009.
- [51] A. C. Kak and M. Slaney, *Principles of Computerized Tomographic Imaging*, IEEE Press, New York, 1988.
- [52] <http://clinical.netforum.healthcare.philips.com/global/Explore/Case-Studies/CT/Routine-brain-scan>.
- [53] Z. Wang, A. C. Bovik, H. R. Sheikh, and E. P. Simoncelli, “Image quality assessment: from error visibility to structural similarity,” *IEEE Transactions on Image Processing*, vol. 13, no. 4, pp. 600–612, 2004.
- [54] Q. Huynh-Thu and M. Ghanbari, “Scope of validity of PSNR in image/video quality assessment,” *Electronics Letters*, vol. 44, no. 13, pp. 800–801, 2008.
- [55] S. V. Mohd Sagheer and S. N. George, “A review on medical image denoising algorithms,” *Biomedical Signal Processing and Control*, vol. 61, p. 102036, 2020.
- [56] F. Sattar, L. Floreby, G. Salomonsson, and B. Lovstrom, “Image enhancement based on a nonlinear multiscale method,” *IEEE Transactions on Image Processing*, vol. 6, no. 6, pp. 888–895, 1997.
- [57] G. Blanchet and L. Moisan, “An explicit sharpness index related to global phase coherence,” *IEEE International Conference on Acoustics, Speech and Signal Processing (ICASSP)*, pp. 1065–1068, 2012.
- [58] A. M. Eskicioglu and P. S. Fisher, “Image quality measures and their performance,” *IEEE Transactions on Communications*, vol. 43, no. 12, pp. 2959–2965, 1995.
- [59] K. Padmavathi, C. S. Asha, and V. K. Maya, “A novel medical image fusion by combining TV-L1 decomposed textures based on adaptive weighting scheme,” *Engineering Science and Technology, an International Journal*, vol. 23, no. 1, pp. 225–239, 2020.
- [60] N. Bharti and S. Chandra, “Image de-noising based on nature inspired optimization algorithm,” *2018 Second International Conference on Computing Methodologies and Communication (ICCMC)*, pp. 697–703, 2018.